

Modelling erosion, entrainment and deposition in cohesive granular flows: Application to dense snow avalanches

Camille Ligneau^{a,*}, Betty Sovilla^a, Johan Gaume^{a,b,c}

^a WSL Institute for Snow and Avalanche Research SLF, Davos, Switzerland

^b Institute for Geotechnical Engineering, ETH Zurich, Zurich, Switzerland

^c Climate Change, Extremes, and Natural Hazards in Alpine Regions Research Center CERC, Davos Dorf, Switzerland

ARTICLE INFO

Keywords:

Gravitational mass flows
Granular cohesive flows
Snow avalanches
Entrainment
erosion
Deposition

ABSTRACT

Gravitational mass movements may erode and/or entrain a significant amount of bed material that can strongly affect the flow dynamics until the moving mass eventually deposits and comes to rest. Snow avalanches generally release on slopes covered by a metastable and thus potentially erodible snow cover that can have a wide range of strength – or cohesion – depending on the type of snow and its physical properties. As the avalanche flows, the snow cover is fully or partially entrained at the front and at the base of the flow, increasing the mass of the avalanche. Conversely, at the tail, snow may be deposited along the track, reducing the overall flowing mass. The balance between entrainment and deposition therefore determines the growing or decaying of the avalanche in terms of mass. To date, it remains unclear how cohesion influences these processes and what consequences it has for avalanche dynamics and run-out. Here, we perform simulations based on the Discrete Element Method (DEM) to analyze the influence of cohesion and slope angle on the erosion, entrainment, mixing and deposition processes. This method makes it possible to follow the dynamics of the particles within the flow very precisely, something that cannot be done in real experiments. In the model, the cohesion is represented as the combined effects of a fragmentation potential associated with the strength of the bonds, and an aggregation potential associated with the stickiness of the particles. For various combinations of input parameters and material properties, we release a heap of particles over an erodible bed and simulate the entrainment and deposition mechanisms. Our results show on the one hand that a low strength (< 3 kPa) promotes a ploughing entrainment mechanism and a large entrainment velocity, up to 3 m/s. On the other hand a high strength (> 3 kPa) favors basal abrasion as the flow front is not able to destabilize the erodible bed at once. In this case, the entrainment velocity decreases typically below 1 m/s. This has important consequences on mixing: the front in granular flows with low strength and adhesion is typically made of freshly entrained material coming from the whole depth of the bed, while remains of the released material can be found at the front of highly cohesive avalanches. Finally, the deposition process is analyzed by evaluating the relationship between the deposit thickness h_{stop} and slope angle θ which extends the framework of the model of $h_{\text{stop}}(\theta)$ from cohesionless to cohesive granular flows. We find that a higher bond strength of the flowing material increases the deposition height. Our work improves our understanding of the mechanics of cohesive granular flows and may contribute to improving parameterizations in depth-averaged models used to simulate geophysical mass flows such as rock, ice, snow avalanches, debris flows and landslides.

1. Introduction

Among the various natural hazards existing in mountainous areas, snow avalanches are one of the most frequent and have a strong damage potential. Their risk is mainly mitigated by efforts to map the avalanche speed, pressures and run-out distance, so that construction in endan-

gered areas can be avoided or sufficiently strong structures can be designed and dangerous zones secured when necessary. These predictions are made with the help of numerical models, usually solving the conservation of mass and momentum in a depth-averaged manner using St-Venant equations (Grigorian et al., 1967; Savage and Hutter, 1989). In such models, basal entrainment or deposition may be included in the

* Corresponding author.

E-mail address: camille.ligneau@slf.ch (C. Ligneau).

<https://doi.org/10.1016/j.coldregions.2023.104103>

Received 24 November 2022; Received in revised form 15 December 2023; Accepted 16 December 2023

Available online 22 December 2023

0165-232X/© 2023 The Authors. Published by Elsevier B.V. This is an open access article under the CC BY license (<http://creativecommons.org/licenses/by/4.0/>).

mass balance, i.e. $\partial_t H + \partial_x(HU_x) + \partial_y(HU_y) = Q(x, y, t)$ where $H(x, y, t)$ is the flow height, $U(x, y, t)$ the velocity vector and $Q(x, y, t)$ the mass flux across the avalanche boundaries. The latter term refers to snow entrainment when its sign is positive and to deposition when its sign is negative. Numerous mathematical models have been proposed to describe the entrainment and deposition processes, with mass change rates usually related to the flow velocity (Eglit and Demidov, 2005), the flow height, the friction and/or the slope angle (Naaim et al., 2003; Sovilla et al., 2010) or the thickness of the erodible bed (Bouchaud et al., 1995; Takahashi, 2001). However, even though a mechanical threshold can be included in such models (Grigorian et al., 1967; Grigorian and Ostroumov, 1977), the question of how the material cohesion affects erosion, entrainment and deposition remains unsolved. Yet, in a warming climate, we expect changes in snow mechanical properties (Steinkogler et al., 2015b) and a higher proportion of wet snow avalanches (Giacona et al., 2021; Naaim et al., 2016; Pielmeier et al., 2013). Thus, a better understanding of the effect of cohesion on the processes of entrainment and deposition is highly needed.

Gauer and Issler (2004) break down the process of removal of bed material by the flow into two conceptual phases. The first phase is called erosion and expresses the breaking up of the snow cover into pieces of various sizes depending on the snow type. The second phase, called entrainment, is the acceleration of this eroded snow by the flow. Conceptual mechanisms of erosion/entrainment of a snow cover are defined for example by Gauer and Issler (2004), namely the particle impact erosion, abrasion, fluidization – later coined as eruption (Lounge et al., 2011) – and ploughing. The latter refers to the entrainment of dense snow at the avalanche front and is recognized to be an important mode of mass intake in snow avalanches (Sovilla et al., 2006). Another process called slab entrainment was hypothesized by Issler et al. (2000) and observed by Köhler et al. (2018a). It corresponds to the sudden detachment and entrainment of a metastable large snow slab located along the avalanche path.

Beyond the fact that the entrained material increases the overall flow mass, it is important to note that it can also change the mechanical properties of the flow if the erodible bed has different properties than the flow. For instance, it has been observed that a higher water content in the bed increases the velocity of debris-flows and landslides (Iverson et al., 2011; Mangeney, 2011), while in snow the formation of granules of various sizes has been related to the snow temperature and liquid water content (Steinkogler et al., 2015b). Therefore, it is also important to study how the entrained material is mixed within the flow after it has been entrained, as it can give precious information on the evolution of the flow dynamics.

In geophysical gravitational flows, entrainment has been experimentally analyzed for landslides and debris flows (Iverson et al., 2011) and for snow avalanches (Sovilla et al., 2006) in terms of impacts on the mass and velocity growth. Recent numerical developments using in particular the Material Point Method allowed some researchers to simulate entrainment in different types of gravitational mass movements at a large scale (Cicoira et al., 2022; Gaume et al., 2018; Gaume et al., 2019; Vicari et al., 2022). However, the mechanisms themselves have been scarcely explored and the experiments have been limited either to cohesionless particles (Barbolini et al., 2005; Edwards et al., 2021; Viroulet et al., 2019) and/or to short erodible beds relative to the flow size (Kang and Chan, 2018; Li et al., 2022), where no steady state could be reached.

Deposition of snow occurs mainly at the tail of the avalanche (Sovilla et al., 2010) but can also be observed on the sides of the flow where levees may form and channel the avalanche (Bartelt et al., 2012; Gray and Thornton, 2005). Sovilla et al. (2010) linked the deposition height h_{stop} to the slope angle θ , following the work of Pouliquen (1999) with dry cohesionless granular flows. However, the role of cohesion is also acknowledged in the deposition mechanism of snow avalanches (Köhler et al., 2018a) but no work has investigated the effect of cohesion on the

$h_{\text{stop}}(\theta)$ curves.

In this article, we investigate the effect of granular cohesion on the processes of erosion, entrainment, mixing and deposition. In the following Section, we describe the methods used to study the processes. Sections 3.1, 3.2 and 3.3 show the results of simulations for entrainment, mixing and deposition, respectively. Finally, Section 4 discusses the results in relation to existing knowledge.

2. Materials and methods

In this section, we describe the methods, setups, parameters and procedures used to simulate and investigate the entrainment of an erodible snow cover by an avalanche flow, as well as the snow deposition at its tail. First, we present the Discrete Element Method (DEM) and the basic parameters used to simulate snow. Then, we introduce the setups and procedures implemented in this work to study entrainment, erosion and mixing, as well as the parameters of cohesion used to mimic various types of snow. The last part is dedicated to the setup and procedure to model deposition using the theory proposed by Pouliquen (1999) for dry granular flows.

2.1. Discrete element method

We model snow by the means of the Discrete Element Method introduced by Cundall and Strack (1979), which consists of simulating an assembly of discrete particles having mechanical parameters tailored to resemble the granular properties of snow. We use the PFC software developed by Itasca Consulting Group, which implements this method. At every timestep of a simulation, Newton's laws of motion are resolved over each particle, and individual positions and velocities can be extracted. A detailed description of the model can be found in Ligneau et al. (2022). Here, we choose to use the 2D configuration of the model in order to reduce the computational time, because of the large number of particles required in simulations. Particles are therefore cylinders with a mean diameter d_p , unit length, and symmetry axes perpendicular to the computational plane.

The way particles interact with each other is set through a contact model and mechanical properties that fit the material behavior. The contact model used in this study is based on the parallel-bond model (PBM) (Potyondy and Cundall, 2004), modified to include the possibility for particles to naturally aggregate. Similar models have been previously proposed to simulate avalanche impact pressures (Kyburz et al., 2022a, 2022b; Kyburz et al., 2020) and snow granulation (Steinkogler et al., 2015b). With this model, the contact between two particles can take two states: unbonded or bonded. The unbonded case consists of a simple visco-elastic frictional contact with a Young's modulus E , a damping coefficient β and a friction coefficient μ_p . The bonded state model comprises the unbonded state model and adds a solid elastic bond between the two particles, which works in parallel with the visco-elastic contact of the unbonded state model. The bond has the same Young's modulus E as the particles and a cross-sectional area equal to the smallest diameter of the two particles in contact. The bond can break if the shear or tensile stress exceeds the bond's shear strength or tensile strength, respectively. In this case and if the particles are still in contact after the breakage, the contact is again treated with the unbonded state model until a new bond is formed or until the two particles move away from each other. The formation of a bond can happen in two ways. First, bonds can be created between touching particles while making the initial state of the simulation, e.g. for the snow cover particles to provide an initial strength (Section 2.2). Second, a bond can be created at any moment during the simulation if the compressive stress pushing two particles together passes over a given threshold σ_{agg} .

The basic set of parameters used in the simulation is taken from Ligneau et al. (2022) and is listed in Table 1. As explained above, snow cohesion results from brittle bonds between particles. The propensity of

Table 1
Main properties of the particles.

Parameters	Symbol	Value / range
Particle diameters	d_p	80 $\mu\text{m} \pm 20\%$
Particle density	ρ_p	350 kg/m^3
Bulk density	ρ_b	260–280 kg/m^3
Young modulus	E	10^6 Pa
Friction coefficient	μ_p	0.5
Damping ratio	β	0.5

bond formation is set by the value of σ_{agg} . On the other hand, the propensity of bond breakage is set by the value of σ_{bond} which is the stress threshold above which a bond will break. We make these quantities dimensionless by scaling them with the maximum hydrostatic pressure in the erodible bed on a flat slope $P_{\text{max}} = \rho_b g h_{\text{eb}}$, with h_{eb} the depth of the erodible bed. Thus, the aggregation number η_{agg} and fragmentation number η_{frag} jointly characterize the cohesion and are defined as:

$$\eta_{\text{agg}} = \frac{P_{\text{max}}}{\sigma_{\text{agg}}} \quad \text{and} \quad \eta_{\text{frag}} = \frac{P_{\text{max}}}{\sigma_{\text{bond}}} \quad (1)$$

It should be noted that a comparison of η_{agg} and η_{frag} with the works of Steinkogler et al. (2015b) and Ligneau et al. (2022) should be carefully made, as they adimensionalize the stress thresholds with the kinetic stress of the particles and the depth-averaged stress, respectively.

2.2. Setups and procedures

2.2.1. Flow over an erodible bed

The setup to investigate entrainment (Fig. 1) consists of two zones having a constant slope θ . In the upstream zone, a granular mass (in purple) is released on a frictionless surface. These particles hit the downstream zone made of an erodible bed of particles (in yellow), framed with particles fixed in translation and rotation (in green). In a given simulation, all particles have exactly the same properties so we assume that the released and erodible particles are made of the same material. The released particles are initially packed in a column of $5 \times 5 \text{ m}^2$, containing about 4000 particles. The length of the release zone is 20 m and was chosen so that the flow reaches approximately 15 m/s when it hits the erodible bed. The thickness of the erodible bed is 1.2 m (≈ 15 particles) and the length is 100 m, chosen to be long enough to reach and maintain a steady propagating flow for at least a few tens of meters. The erodible bed is prepared on a horizontal slope ($\theta = 0^\circ$) by ballistic deposition of particles. During this preparation step, the particles are not allowed to bond in order to avoid the formation of loose, fragile and unstable structures within the erodible bed (Kadau and Herrmann, 2011). A volume fraction of approximately 0.75 is attained.

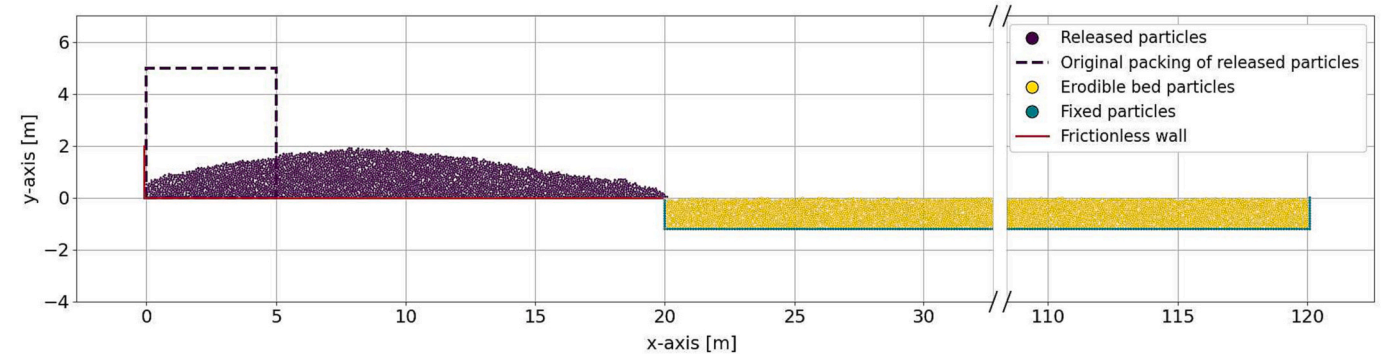


Fig. 1. Setup used in the simulations to investigate entrainment, mixing and deposition. An initial avalanche is generated by releasing a heap of particles (purple) on a frictionless wall (red solid line). It then runs into an erodible bed (yellow) which is framed by particles fixed in rotation and translation (green). Here, the state of the system is shown just before the first particle from the release hits the erodible bed. (For interpretation of the references to colour in this figure legend, the reader is referred to the web version of this article.)

Then, all the contacts are changed from the *unbonded* state to the *bonded* state (i.e. a bond of strength σ_{bond} is added to each contact between particles), regardless of the value of σ_{agg} and of the compressive stress between the two particles in contact. This provides an initial strength and stability to the erodible bed. Finally, the gravity is gradually tilted to reach the desired slope angle. For our set of particle properties given in Table 1 and for each couple $[\eta_{\text{frag}}; \eta_{\text{agg}}]$, a range of slope angles $[\theta_{\text{stop}}, \theta_{\text{start}}]$ exists where the flow can develop to a steady state. If the slope angle is below θ_{stop} , the flow decelerates and eventually stops. At the other end, if the slope angle is greater than θ_{start} , the bed is unstable and starts to flow only under the gravitational force (GDR MiDi, 2004). Because the present work aims to study steady propagating flows, it is therefore important that the slope angle is comprised between θ_{stop} and θ_{start} . The Section 2.2.2 explains how these ranges are determined.

When the released particles hit the erodible bed, a transition phase is observed before a steady state is established (Fig. 2). During this phase, the flow properties, such as the velocity and flow height, adapt to the newly encountered ground conditions. In this study, we leave this phase aside to focus only on the steady state regime. In all simulations, steady state is reached after the flow front exceeds the distance $x = 80$ m, regardless of the slope and cohesion used. Therefore, all results presented in this article are computed for the range $80 \text{ m} < x < 115$ m, where the upper value is chosen to be 5 m before the end of the domain to avoid border effects.

We explore the effect of cohesion through four cases (Table 2), which correspond to low and high values for η_{agg} and η_{frag} . A high value for η_{agg} denotes a high rate of bond formation, i.e. the particles become very sticky, or adhesive. Therefore, we name *high adhesion* the cases with a high η_{agg} . Conversely, we use *low adhesion* for the cases with a low η_{agg} , which means that bonds are not likely to form during the simulation. Furthermore, we name *low* or *high strength* the cases with a high and low η_{frag} , respectively (a low strength means a high fragmentation potential and vice versa). Combinations of the two parameters will then define different snow property scenarios. Specifically, the *low adhesion–low strength* case is representative of a dry loose snow inducing a cold dense regime (Köhler et al., 2018a; Ligneau et al., 2022). The *low adhesion–high strength* case depicts a stronger snow in its initial state but the low η_{agg} prevents the formation of new bonds, making the simulated material comparable to a brittle snow slab. The *high adhesion–low strength* case models a moist or wet snow, where the presence of liquid water favors the formation of weak capillary bonds between snow grains. Finally, the *high adhesion–high strength* case gives the most intense cohesion to the particles and illustrates a heavy compacted snow found e.g. in avalanche deposits. A mechanical analysis of the bulk properties (failure envelope and $\mu(I)$ rheology) of each case is given in Appendix A.

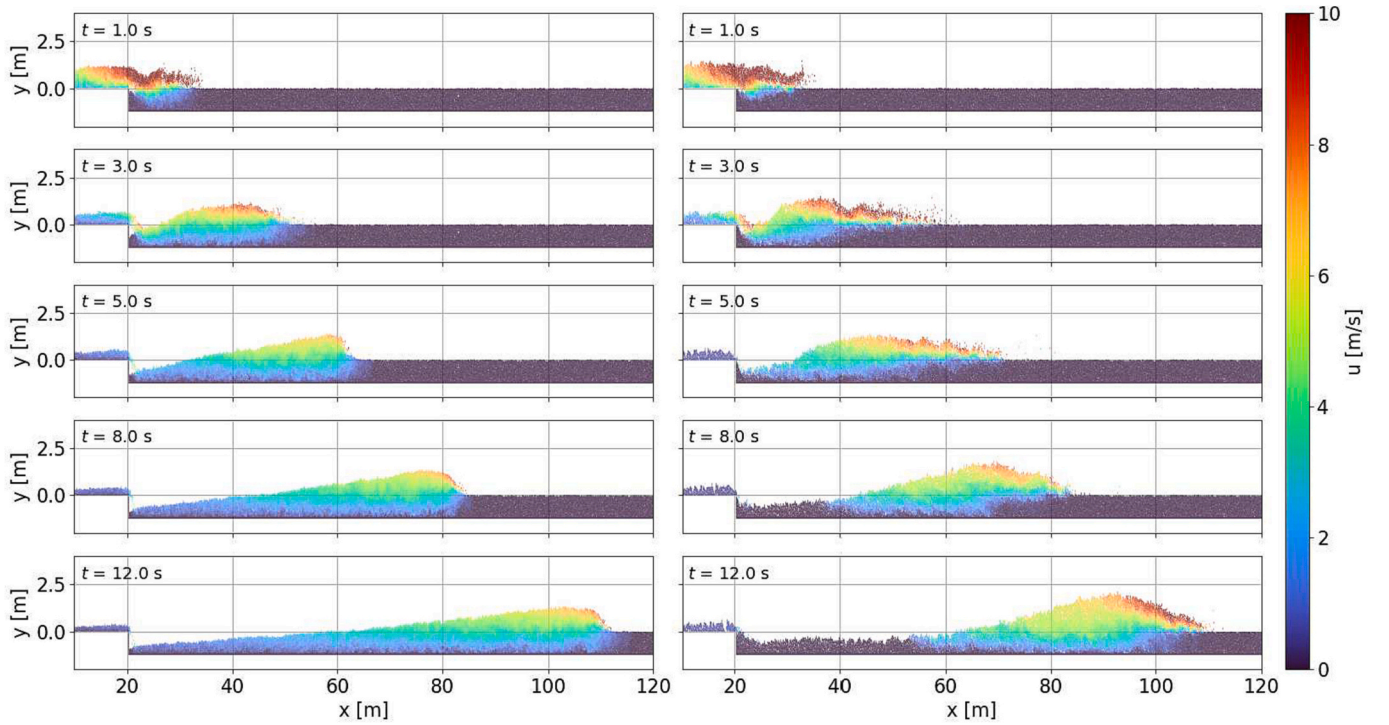


Fig. 2. Simulation of the *low adhesion–low strength* (left) and a *high adhesion–high strength* (right) scenarios. Colors represent particle velocities for $t = 1, 3, 5, 8$ and 12 s after the first flowing particles hits the erodible bed. The parameters used in the simulations are listed in Table 2.

Table 2

Cohesion properties and slope angle θ for the four representative cases.

Portrayed snow state	Comparable to	η_{frag}	η_{agg}	σ_{bond} [kPa]	σ_{agg} [kPa]	Slope angle θ in simulations [°]
<i>low adhesion–low strength</i>	Loose new snow	3	0.1	1.1	21.2	20
<i>low adhesion–high strength</i>	Brittle slab	0.75	0.1	4.2	21.2	26
<i>high adhesion–low strength</i>	Moist or wet snow	3	7.5	1.1	0.4	32
<i>high adhesion–high strength</i>	Avalanche deposit	0.75	7.5	4.2	0.4	30

2.2.2. $h_{\text{stop}}(\theta, \sigma_{\text{bond}})$ and $h_{\text{start}}(\theta, \sigma_{\text{bond}})$

As explained in Section 2.2.1, the inclination of the erodible bed must be within the range $[\theta_{\text{stop}}, \theta_{\text{start}}]$ to be in a metastable state. This range depends on the height of the erodible bed h_{eb} and also on the cohesion, as we will show in Section 3.3. Previously, we have defined cohesion as a combination of potentials of aggregation and fragmentation. In contrast here we analyze only the potential for aggregation to better understand the effect of the strength σ_{bond} . Therefore, we need to describe the relations $h_{\text{stop}}(\theta, \sigma_{\text{bond}})$ and $h_{\text{start}}(\theta, \sigma_{\text{bond}})$. Moreover, the curve of $h_{\text{stop}}(\theta, \sigma_{\text{bond}})$ is important to characterize the deposition processes at the avalanche tail, as it provides the height of deposition and thus can be correlated with mass loss. The numerical setup to obtain h_{stop} and h_{start} consists of a layer of particles of dimensionless height h/d_p deposited on a rough plane made of the same, but fixed, particles. Periodic boundary conditions are applied on the lateral sides to allow the particles to flow continuously. The slope angle θ is varied by changing the direction of gravity.

The initial state is made by depositing particles on the rough plane with $\theta = 0^\circ$, until the desired height is reached. Like for the preparation of the erodible bed explained in Section 2.2.1, particles are not allowed to bond during this phase but all the particles in contact are bonded once the arrangement is finished. We choose to simulate 15 different values of h/d_p in the range 2–30, which corresponds in our case to heights in the range 0.08–2.4 m. This extent is sufficient to observe the effect of cohesion on h_{stop} and h_{start} , and to propose an empirical equation fitting the results.

First, θ is increased incrementally until the particles begin to flow. The value of θ_{start} matches the slope for which the average particle velocity \bar{u} reaches the arbitrary threshold $\bar{u} \geq 0.2$ m/s. This velocity also represents the threshold that we use to separate entrained particles and static ones in all our simulations. We choose to limit the angle at a maximum value of $\theta_{\text{max}} = 50^\circ$. From θ_{start} , the angle is then gradually decreased. The value of θ_{stop} matches the slope for which the average particle velocity \bar{u} reaches the value $\bar{u} \leq 0.01$ m/s. In the case where θ_{max} is reached before the flow starts (which happens for high values of σ_{bond}), a lightly sheared velocity profile is imposed on the particles, simply to trigger the flow. The angle increments/decrements consist of slow steps of $\pm 0.1^\circ$ every 0.5 s, which gives a satisfactory balance between the resolution on θ and the computational time. Additional individual decrements of 5° to 15° were sometimes used during the search for θ_{stop} in order to decrease the computational time and avoid a overly large momentum of the particles.

3. Results

3.1. Entrainment

In the simulations presented in Fig. 2, we can distinguish two primary mechanisms of entrainment, depending on slope angle and cohesion: ploughing (left panels) and abrasion (right panels). Ploughing is characterized by the fact that static particles are set in motion downstream of the flow front (Fig. 3a,c). On the other hand, abrasion is characterized by the entrainment of particles below the avalanche front

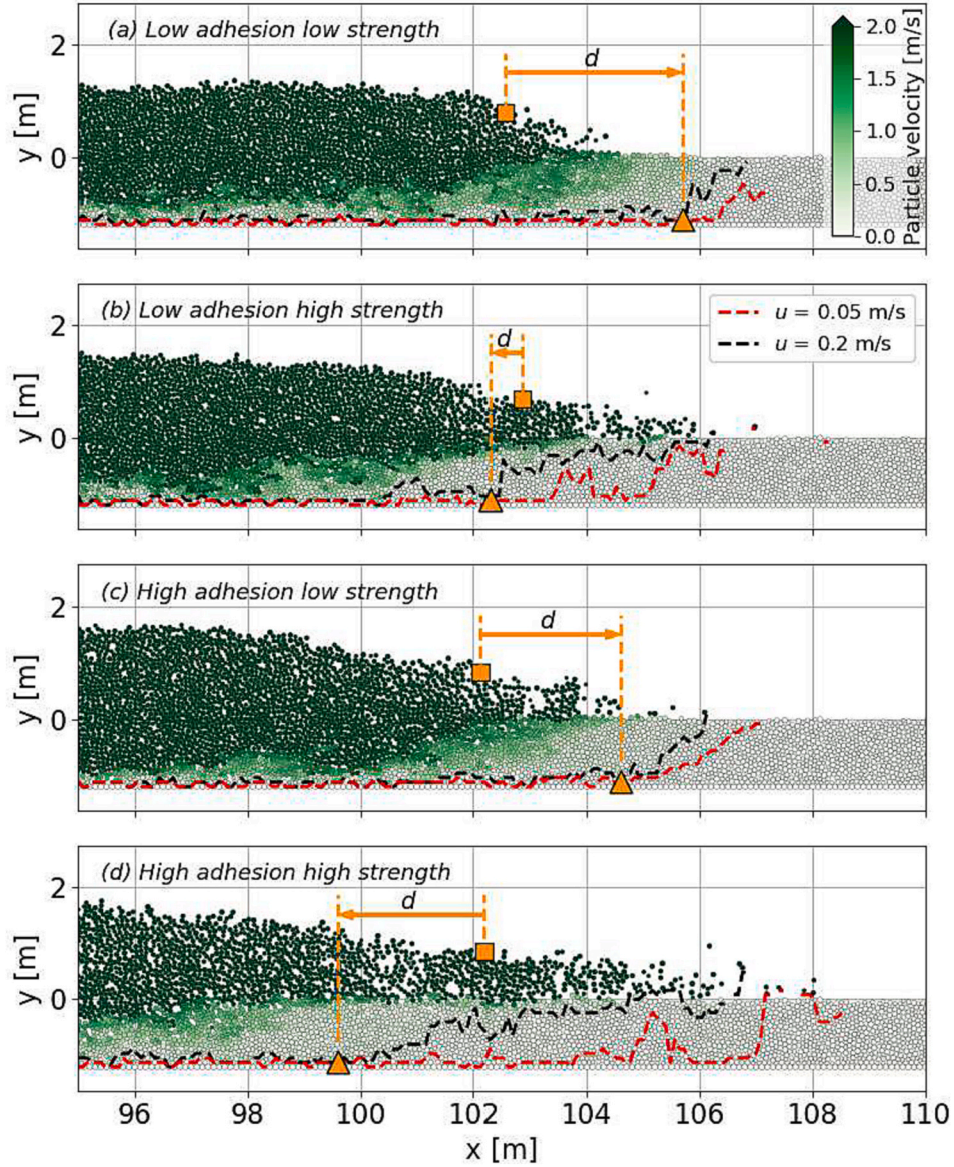


Fig. 3. Detail of the particles at the flow front during the steady state. The panels depict the four snow scenarios defined in Table 2. The gradient of greens indicates the velocity values (up to 2 m/s). The red dashed line shows the limit where $u=0.05$ m/s and the black dashed line indicates the entrainment limit $u=0.2$ m/s. The orange squares and triangles display the positions of the flow front and the position where the whole depth of the erodible bed is entrained, respectively. Two entrainment processes can be observed: ploughing and abrasion. (For interpretation of the references to colour in this figure legend, the reader is referred to the web version of this article.)

and body (Fig. 3b,d). In our simulations, the whole depth of the erodible bed is always entrained at some point. To determine which process is occurring and its intensity, we define the distance $d = x_e - x_{ff}$, taken along x (i.e. parallel to the ground), corresponding to the distance between the flow front and the position where the entire bed depth is eroded. We estimate the position of the flow front x_{ff} (orange squares in Fig. 3) by computing the center of mass of the 30 fastest particles of the flow. This arbitrary criterion proved to be reliable for all simulations, as the maximum velocity of the flow is always situated at the front. The position x_e , where all the bed's depth is entrained, is assessed by measuring where the velocity of the deepest layer grows above the threshold $u=0.2$ m/s. It is represented by the orange triangle in Fig. 3. If $d > 0$, the entrainment front is located downstream of the avalanche front, therefore ploughing occurs, while if $d < 0$ the entrainment front is located upstream of the avalanche front and particles are mostly entrained by abrasion.

The computed values of d are shown in Fig. 4 for several bond

strengths σ_{bond} and slope angles θ . The left graph shows values of d for a low aggregation potential η_{agg} (*low adhesion*), while the right graph gives values for a high η_{agg} (*high adhesion*). With an increasing bond strength, we observe a non-linear decrease in d . For the *low adhesion* cases, d takes positive values for $\sigma_b \lesssim 4.0, 5.0$ and 7.5 kPa, for $\theta = 28^\circ, 32^\circ$ and 36° , respectively, the maximum values being $d = 3.5$ m for $\sigma_b = 4$ kPa and $\theta = 36^\circ$. The distance decreases to approximately -10 m for $\sigma_b = 10$ kPa. For the *high adhesion* cases, d is positive for $\sigma_b \lesssim 2.0, 3.5$ and 4.5 kPa, for the three slope angles. The minimum value in this case is $d = -28$ m for $\sigma_b = 7$ kPa and $\theta = 36^\circ$. Considering the standard deviation of d displayed by the error bars in Fig. 4, the slope angle does not seem to have an important effect compared to the bonds' strength.

A good indicator for quantifying the effect of cohesion on the mass influx of particles into the flow is the entrainment velocity u_e , which is defined as the velocity at which the entrainment front descends in the depth of the erodible bed. We define the entrainment front $h_e(x, t)$ based on the threshold $u(x, y, t) = 0.2$ m/s. This front is illustrated for a given

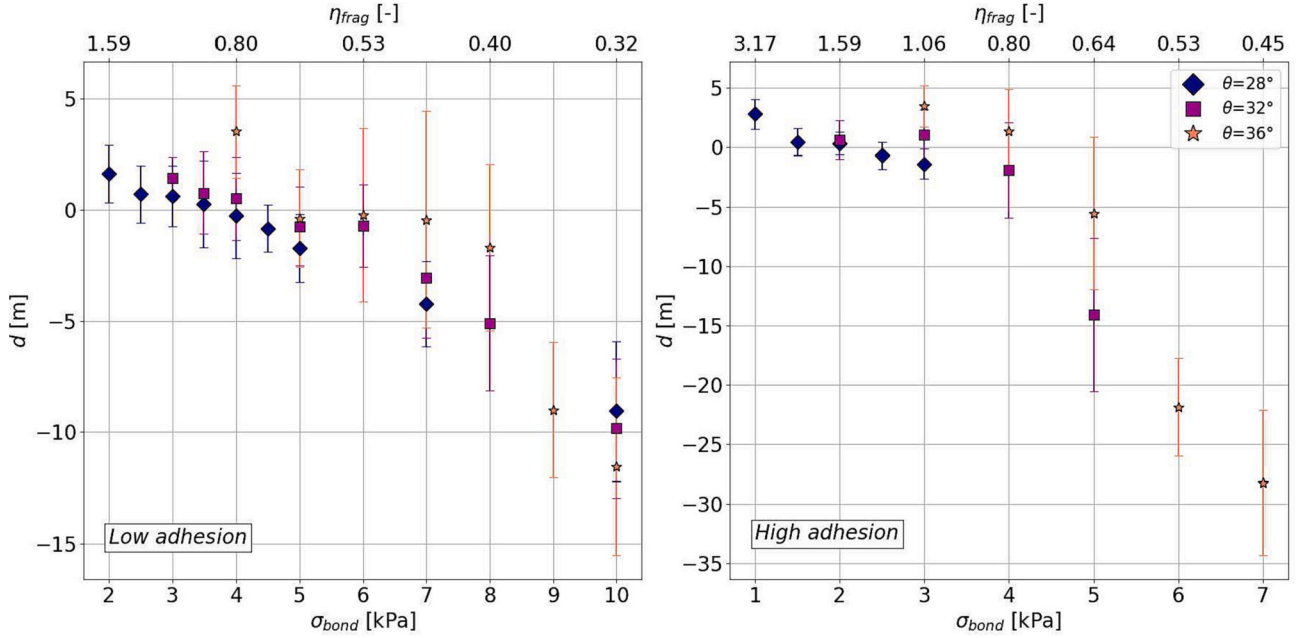


Fig. 4. Horizontal distance d between the flow front and the position where the whole depth of the erodible bed is entrained (orange squares and triangles in Fig. 3) as a function of bond strength σ_{bond} , fragmentation potential η_{frag} and slope angle θ . Values of d are given for a low (left) and high η_{agg} (right).

time step t in Figs. 3 and 7 (black dashed line), and for a given position x in Fig. 5 (black solid line). For each simulation, we estimate an average entrainment velocity \bar{u}_e while the flow is in a steady state. To do so, we first compute the entrainment front $h_e(\tilde{t})$ at regular intervals $\Delta X = 1$ m in the range $x = 80$ –115 m where we consider the flow to be in a steady state (Section 2.2.1). \tilde{t} is the relative time from which the first upper layer of particles is entrained. Then, a linear approximation $\bar{h}_e(\tilde{t})$ of $h_e(\tilde{t})$ is made from $\tilde{t} = 0$ to the full-depth entrainment time (blue dashed line in Fig. 5). The slope of $\bar{h}_e(\tilde{t})$ gives the local time-averaged entrainment velocity. Thus, for one simulation, the entrainment velocity \bar{u}_e is given

by:

$$\bar{u}_e = \frac{\Delta X}{x_{\text{max}} - x_{\text{min}}} \sum_{x=x_{\text{min}}}^{x_{\text{max}}} \bar{h}_e(x, \tilde{t}) \tilde{t} \quad (2)$$

where $x_{\text{min}} = 80$ m and $x_{\text{max}} = 115$ m. The values of \bar{u}_e are shown in Fig. 6 for low (left) and high (right) η_{agg} . The entrainment velocity tends to zero as σ_{bond} increases. Typical entrainment velocities vary between approximately -3 m/s and -0.5 m/s for the *low adhesion* cases, and between roughly -2.2 m/s and 0 m/s for the *high adhesion* case. We note that when $d > 0$, i.e. when ploughing occurs, then $u_e > -2$ m/s.

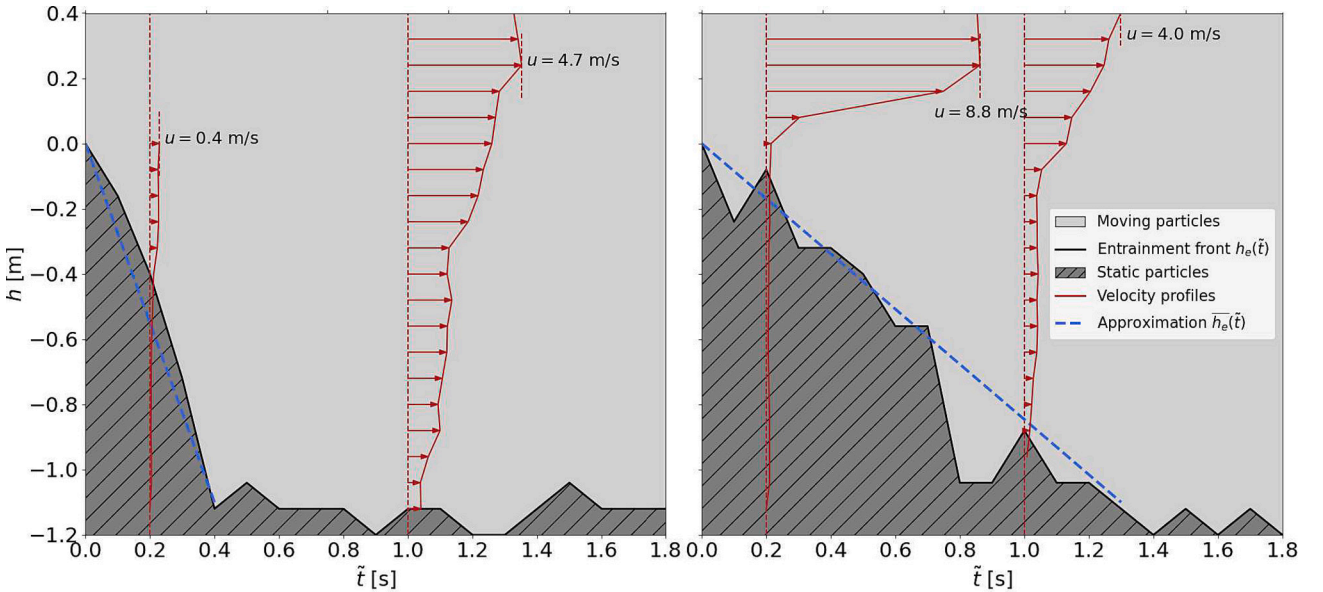


Fig. 5. Location of the entrainment front $h_e(\tilde{t})$ (black line) in time, separating the entrained particles from the static particles, for the *low adhesion-low strength* (left) and the *high adhesion-high strength* cases (right). The x-axis \tilde{t} corresponds to the time after the first layer of particles is entrained. Two velocity profiles are shown for $\tilde{t} = 0.2$ s and 1.0 s, and their maximum velocity in the visible range is annotated. The approximation $\bar{h}_e(\tilde{t})$ of the height of the entrainment front, used to compute u_e , is shown with the dashed blue line. This figure is inspired by a figure in Issler and Pastor Pérez (2011). (For interpretation of the references to colour in this figure legend, the reader is referred to the web version of this article.)

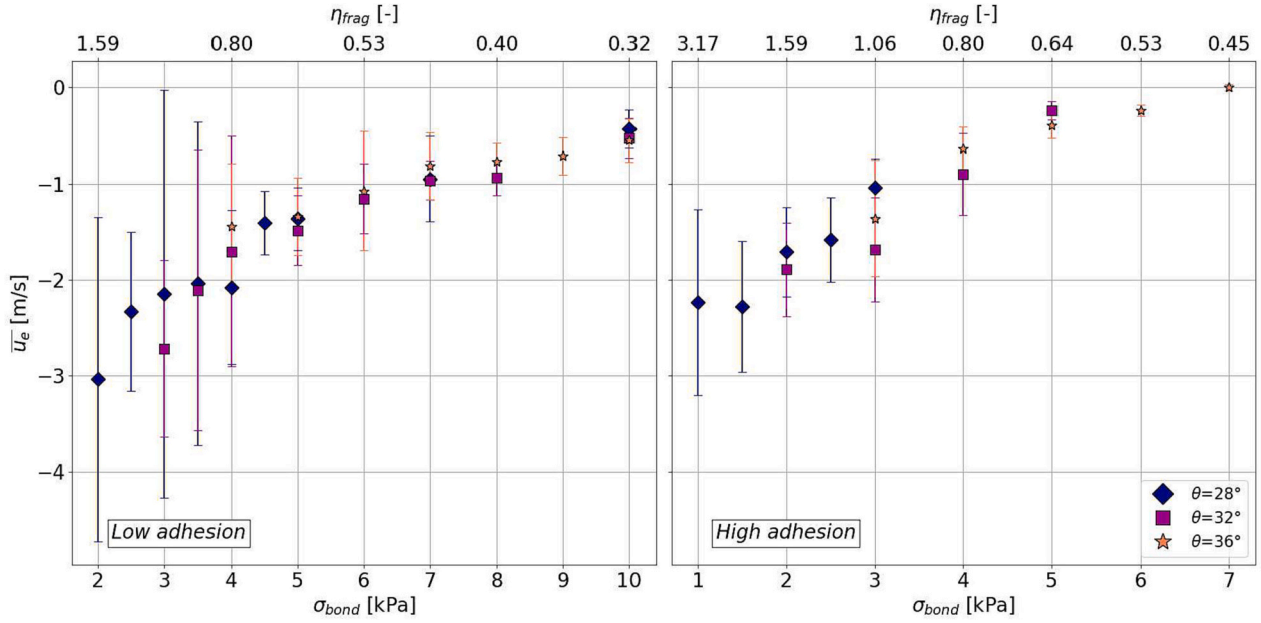


Fig. 6. Entrainment velocity \bar{u}_e for $\eta_{agg} = 0.1$ (left) and $\eta_{agg} = 5.0$ (right).

3.2. Mixing

In natural gravity flows, the properties of the materials composing

the erodible bed and the avalanche are not necessarily the same. Therefore, it is important to understand how particles that were originally static are mixed inside the avalanche, as this may affect the me-

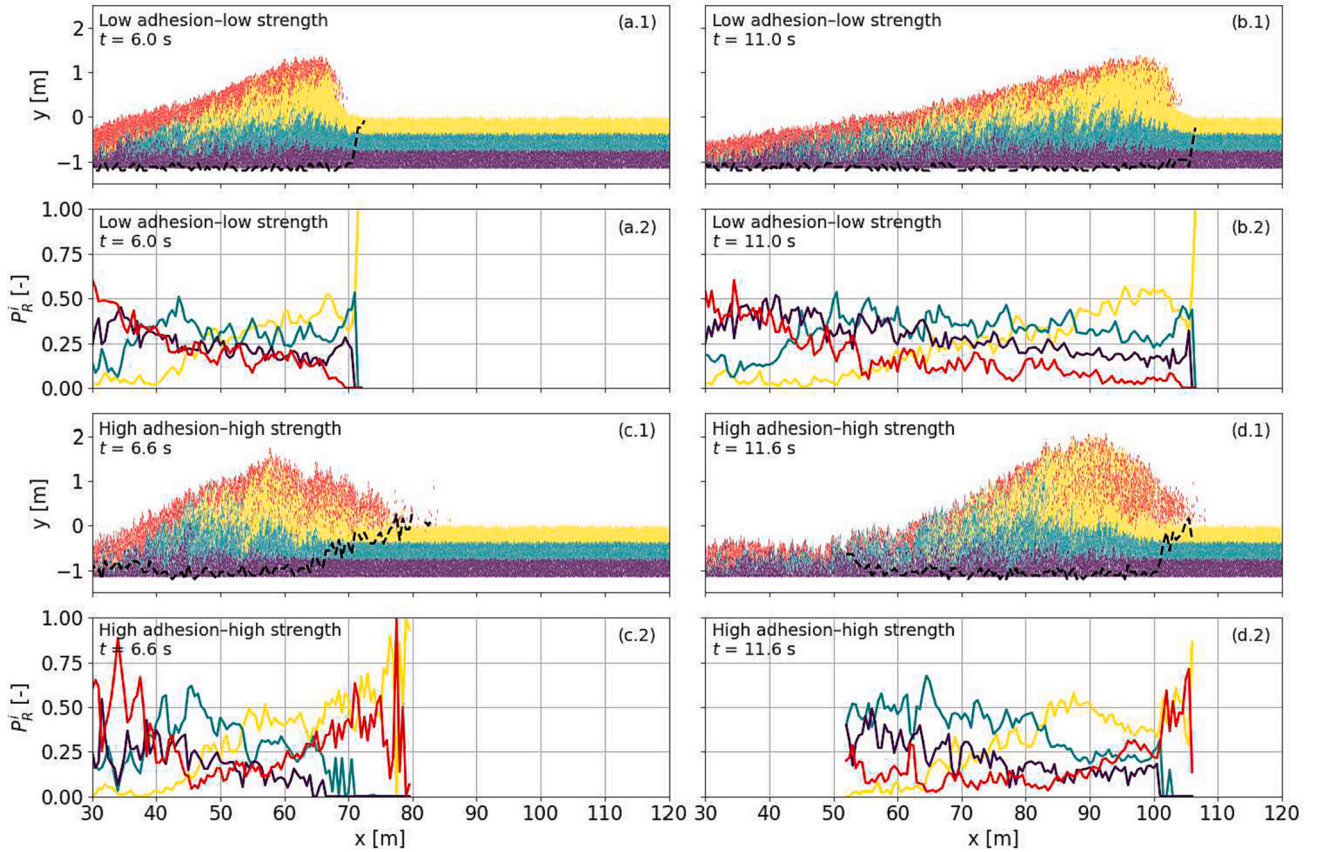


Fig. 7. Panels (a,b.1) display screenshots of the *low adhesion-low strength* scenario and panels (c,d.1) of the *high adhesion-high strength* scenario. The particle colors are a function of their initial depth in the erodible bed (yellow, green and purple), and the red particles are those from the original release. The dashed black line indicates the position of the entrainment front corresponding to a velocity threshold of $u = 0.2$ m/s. Panels (a-d.2) show the particle ratio P_R^i for each layer i along the length of the flow, for the corresponding (a-d.1) panels. (For interpretation of the references to colour in this figure legend, the reader is referred to the web version of this article.)

chanical properties of the avalanche. In our simulations, the bed and the avalanche are made of the same material, but we can still qualitatively observe the mixing processes between the entrained snow and the avalanche by using particle colors as tracers, for the *low adhesion–low strength* and *high adhesion–high strength* cases. Fig. 7 shows how the particles are distributed in the avalanche, depending on their initial depth in the snow cover. In panels (a–d.1) of Fig. 7, three layers of thickness 0.4 m are displayed in different colors over the initial depth of 1.2 m: the surface layer (yellow), the middle layer (green) and the deep layer (purple). The particles coming from the release are shown in red. Panels (a–d.2) show the particle ratios $P_R^i(x) = N_i(x)/N_{total}(x)$ of each initial layer i along the flow length with a resolution $\Delta x = 1$ m. In the following, i takes the labels S, M, D and R , for the surface, middle, deep layers and the released particles, respectively. To compute the ratio, only the particles with a velocity higher than 0.2 m/s are counted. The entrainment front threshold is shown with the black dashed line in (a–d.1). Panels (a,b) correspond to the *low adhesion–low strength* case and (c,d) to the *high adhesion–high strength* case (Table 2). Both cases are shown at two different timesteps in order to visualise the evolution of the flow.

In the *low adhesion–low strength* case, the surficial part of the flow at $t = 6$ s is essentially composed of particles coming from the release (Fig. 7a.1), but they are slowly replaced by particles from the erodible bed (Fig. 7b.1). For example, at the front (i.e. roughly the 10 first meters of the avalanche), P_R^R diminishes from about 0.2 to 0.1, while P_R^S increases from about 0.4 to 0.5 (Fig. 7a.2, b.2). We note that P_R^S is maximum at the front and decreases towards the tail to reach almost a null value. In contrast, P_R^D grows towards the tail, just like the proportion of particles from the release P_R^R . In between, P_R^M is maximum a few dozen meters behind the front and then fades at the tail. Previously, we have seen that the entrainment occurs as ploughing in this case, with a very high entrainment velocity. After the entrainment, the layering structure of the original snow cover can still be recognized in the avalanche, indicating that the vertical mixing is not so strong.

For the *high adhesion–high strength* case, the trend of the surface layer is similar to that of the *low adhesion–low strength* case: P_R^S is maximum at the front and then decays towards the tail. The trends of the intermediate and deep layers are also similar, but show a faster change along x because the total length of the flow is much shorter (about 60 m versus

more than 80 m). The main difference lies in the higher proportion of released particles P_R^R that stay at the front in the *high adhesion–high strength* case (c,d.2). In addition, at the front, the flow is composed only of particles from the surface layer and the release. This is because the low entrainment velocity of abrasion prevents the flow front from entraining particles from the intermediate and deep layers. This process increases vertical mixing within the flow, as observed by the difference in the preservation of the original bed stratification between panels (b.1) and (d.1).

To get a better idea of the specific areas where mixing occurs within the flow, we compute the granular temperature T_g , which is a measure of the velocity fluctuations and illustrates the random motion of the particles. This quantity is estimated as:

$$T_g(x, y) = \frac{\text{tr}(\sigma_k(x, y))}{2\rho(x, y)} \quad (3)$$

where $\sigma_k(x, y)$ and $\rho(x, y)$ are respectively the kinetic contribution to the stress tensor and the mass density field as they are defined by Weinhart et al. (2013). Appendix B details the computation of T_g . For the *low adhesion–low strength* conditions (Fig. 8, top), we observe two zones where mixing is maximum. The first is located at the avalanche front, with a length of a few meters and situated above the height of the erodible bed. The second is close to the ground along most part of the flow, but only starting from a few meters behind the front. Milder mixing occurs in the rest of the flow, but no zone is left out. For the *high adhesion–high strength* conditions (Fig. 8, bottom), the contrast between agitated and stagnant areas is more pronounced. We find again the same agitated areas as in the previous case, with the frontal mixing being more intense and spreading over a larger distance behind the front (about a dozen meters). On the other hand, we also identify two zones where T_g drops to low values, even though the particles are flowing. One is close to the ground at the front and is made of the recently-entrained particles. The other is located at the back of the wave, in the range $x = 75$ –90 m and above the height of the erodible bed.

3.3. Deposition

This section explores the effect of cohesion on the height of the deposition at the tail of the avalanche. In past studies on granular flows,

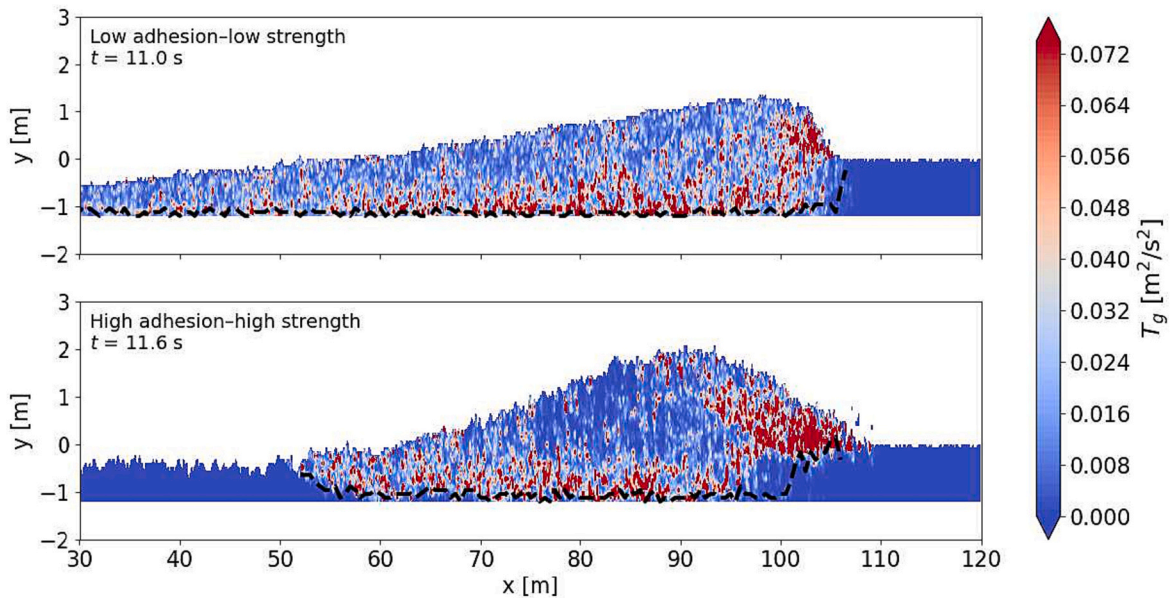


Fig. 8. Granular temperature $T_g(x, y)$ for the *low adhesion–low strength* (top) and *high adhesion–high strength* (bottom) cases. The dashed black line indicates the position of the entrainment front corresponding to a velocity threshold of $u = 0.2$ m/s.

this height h_{stop} has been related to the inclination of the slope θ and the flow height. Here, we run simulations inspired by the experiments of Pouliquen (1999), described in Section 2.2.2, with cohesion between the particles. A sensitivity analysis is performed with regard to the bond strength σ_{bond} , which is varied between 10^{-3} kPa and 10 kPa. The effect of the aggregation potential η_{agg} is not explored here, but we choose a fixed value of $\sigma_{\text{agg}} \approx 10$ Pa (i.e. a high aggregation potential) so that bonds are always formed when two particles come in contact. Fig. 9a shows the curves of $h_{\text{stop}}(\theta)/d_p$ for eight values of σ_{bond} . It can be seen that for increasing σ_{bond} , the curve of $h_{\text{stop}}(\theta)$ shifts to higher angles. Therefore, the deposition height increases with cohesion for a given slope angle. Yet, the shifting magnitude seems to diminish towards high bonds' strength. For instance, for $h/d_p = 10$, the span of θ_{stop} is 11° for $10^{-3} < \sigma_{\text{bond}} < 5$ kPa, whereas it is only 4° for $5 \text{ kPa} < \sigma_{\text{bond}} < 10$ kPa.

In Fig. 9(a,b), each curve is fitted with the relation of GDR MiDi (2004):

$$\frac{h(\theta)}{d} = L \frac{\tan\theta_2 - \tan\theta}{\tan\theta - \tan\theta_1} \quad (4)$$

where the parameters θ_1 , θ_2 and L depend on the properties of the particles and the ground. The diamond markers in Fig. 9(c-e) show the values of these fitting parameters for h_{stop} . They all increase with σ_{bond} and seem to tend towards a maximum value, confirming the previous observation that increased cohesion leads to greater deposition depths. For example, for a slope angle of 30° , the thickness of the deposit of cohesionless flows is about 0.4 m, while it is around 1.6 m for cohesive flows. We also observe that the fitting parameters for the case where $\sigma_b = 10^{-3}$ kPa do not properly match with the trend of higher strength values. It may indicate different deposition mechanisms for very low

cohesion values, but this aspect was not investigated further. Finally, note that our simulation procedure allows us to obtain $h_{\text{start}}(\theta)$ (Fig. 9b), although it is not of primary interest here. We note a similar shape and trend of the $h_{\text{start}}(\theta)$ and $h_{\text{stop}}(\theta)$ curves with a difference for a given angle, which increases significantly with increasing cohesion.

4. Discussion

4.1. Modelling approach and relation to snow properties

The method presented allows to naturally reproduce the interactions between the erodible bed and the flow with a high level of detail and accuracy, which is difficult to achieve in field or laboratory experiments. However, caution must be used when comparing the simulated particles, either static or flowing, with real snow. Indeed, some simplifications had to be made, given the high variability of snow properties from one avalanche to another and also often within a single avalanche.

A first issue concerns the size of the particles in the simulations compared with the actual size of snow granules found in dense avalanches, which can differ considerably between cold dry-snow and warm wet-snow avalanches. Ideally, the size of the simulated particles would have to be about two orders of magnitude smaller, so bigger granules made of particle aggregates would naturally form in the flow because of the cohesive contact model, like in Steinkogler et al. (2015b). However, the computational effort required to simulate the corresponding significant number of particles with DEM is too high, so a balance had to be found between an acceptable computational time and realistic simulations. We chose the mean particle diameter $d_p = 80$ mm in accordance with Bartelt and McArdell (2009) who found median granule sizes of 59–92 mm and 82–162 mm in the deposits of dry and wet avalanches,

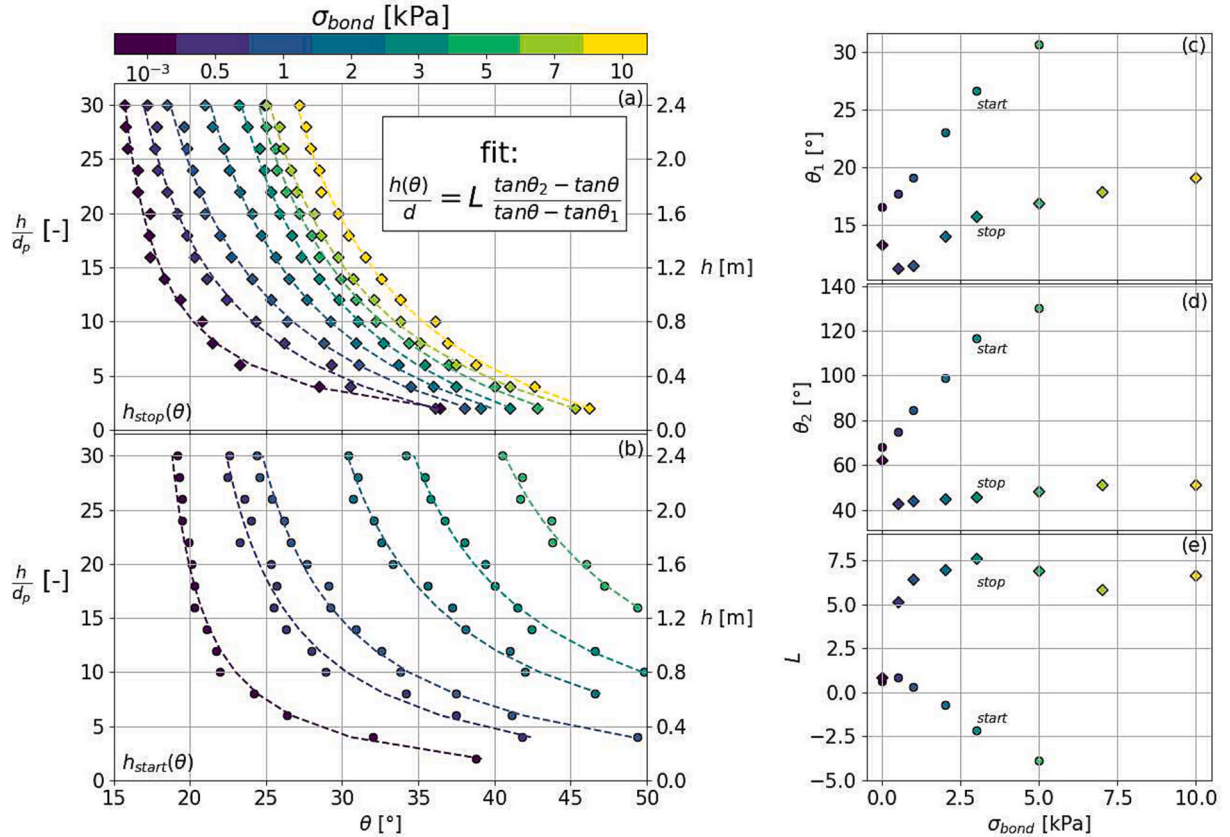


Fig. 9. Curves of (a) $h_{\text{start}}(\theta)$ and (b) $h_{\text{stop}}(\theta)$ for $\sigma_{\text{agg}} \approx 10$ Pa and σ_{bond} in the range 10^{-3} to 10 kPa. In (a,b), the left ordinate-axes show the dimensionless height h/d and the right ones show the actual height h for the mean particle diameter $d_p = 80$ mm in our simulations. The fitting parameters θ_1 , θ_2 and L are plotted in (c–e) for h_{start} (○) and h_{stop} (◊). The colors depict the magnitude of the bond strength σ_{bond} according to the colorbar in the top left.

respectively. The resulting description of the avalanche therefore consisted of a discretisation of the flow, where each discrete element represented a snow aggregate. The validity of this simplification is supported by previous simulations of dense snow flows with DEM (Kyburz, 2021; Ligneau et al., 2022), and by studies that managed to reproduce the run-out area of experimental and natural events of granular mass movements, mostly landslides, with oversized particles (Li et al., 2012; Lo et al., 2011; Thompson et al., 2009). Also, some studies point out that a proper calibration of the DEM parameters (e.g. Young's modulus, friction) leads to realistic results despite the oversizing of the particles (Obermayr et al., 2014; Ucgul et al., 2014). However, it is important to mention that the discretization assumption with large particles is only applicable to the dense parts of the flow. Indeed, the volumetric particle concentrations in the dilute parts of the simulated flow do not match real observations (e.g. the dilute front of the *low adhesion–high strength* and *high adhesion–high strength* scenarios in Fig. 3). In particular, the particle size and volumetric particle concentration could have an important effect on the force chains and would have to be investigated in any future work involving a study of the stress distribution in the erodible bed.

A second point is the ability of the contact model to reproduce various types of snow. Steinkogler et al. (2015b) calibrated the present granular model by linking η_{frag} and η_{agg} to the mechanical and physical properties of actual snow granules formed in a rotating tumbler where the temperature and water content were measured. Furthermore, Ligneau et al. (2022) linked the fragmentation and aggregation potentials to typical flow regimes of snow avalanches by comparing velocity profiles. The two potentials are dependant only on the forces acting at the contact point but not on the contact time, which is an important parameter for dry contacts (Bahaloo et al., 2022). This emphasizes even more that our model is not valid for dilute or semi-dilute flows where particles are in contact for a very short period. Even though the present definition of η_{frag} and η_{agg} varies slightly from that of Ligneau et al. (2022) (σ_{bond} is compared here to the basal hydrostatic pressure instead of the depth-averaged pressure), the order of magnitude is conserved and a direct comparison is still reasonable. Accordingly, our scenarios *low adhesion–low strength* and *low adhesion–high strength* correspond to a cold dense regime (Köhler et al., 2018a; Ligneau et al., 2022). The *high adhesion–low strength* and *high adhesion–high strength* scenarios both relate to a warm shear regime but with different cohesions.

Finally, it is important to note that η_{frag} and η_{agg} are constant in space and time during one simulation, thus the strength of the bonds and the adhesion of particles are the same in the erodible bed and the released mass. This constrains the validity of our simulations only to cases where the cohesion is the same from release to runout, and thus could be a limiting factor when simulating transitional avalanches that change flow regimes along the path due to different snowpack characteristics at low elevations (Köhler et al., 2018b). Also, the cohesion parameters in a simulation are targeted to reach a certain flow regime. For example, σ_{bond} in the *low adhesion–low strength* case is targeted at a cold dense regime. Thus, the cohesion of the erodible bed is aligned with the desired flow regime.

4.2. Entrainment mechanisms

Our computational scenarios reproduce the interaction between dense granular flows and an erodible bed, where the granules are mainly characterized by different values of cohesion. The simulations clearly show the erosion/entrainment mechanisms of ploughing and abrasion. Ploughing is the dominant erosion mechanism for conditions of low strength. In these cases, the force exerted by the avalanche at the front easily breaks particle contacts in the bed ahead of the flow, even before the avalanche arrives (Fig. 3a,c). Almost all the mobilized (eroded) particles are also entrained in the flow with $\bar{u}_e > 2$ m/s, in agreement with the high entrainment rates from the experimental measurements of

Sovilla et al. (2006). Nevertheless, the velocity of our granular flows is lower than the typical real dry-snow avalanche, and since \bar{u}_e should drop as the flow velocity increases, we expect that in real dry avalanches the typical \bar{u}_e could be smaller than in our simulations. The avalanche head is composed mainly of particles from the bed surface or original release. However, as the avalanche propagates, the released particles are deposited and their ratio in the flow decreases. These results confirm the observations of Viroulet et al. (2019), who noted the same behavior in laboratory experiments with granular flows. This implies that frontal avalanche dynamics are dominated over time by the mechanical characteristics of the particles that were initially in the upper layers of the bed. This is particularly important for snow avalanches because the properties of the snowpack can change strongly along the avalanche path as air temperature and thus snow temperature increase at lower elevations (Köhler et al., 2018b; Steinkogler et al., 2015a). Therefore, the mechanical properties of an avalanche can change over time, affecting its mobility and destructive potential.

As the strength of the bonds increases, the dominant entrainment mechanism gradually shifts from ploughing to abrasion. Stronger bonds offer greater resistance to erosion/entrainment, with entrainment occurring mainly in layers that are overridden by the avalanche (Fig. 3b, d). Entrainment velocities u_e are below 1 m/s in agreement with values postulated by Issler and Pastor Pérez (2011) and Gauer and Issler (2004) for snow avalanches. In this case, the frontal dynamic of the avalanche is still controlled by the properties of the surface layer of the bed. However, we also observe that particles from the initial release are still widely present at the front of the avalanche, but they are strongly mixed with the entrained material so it is not likely that they kept their initial properties.

Our simulations show that cohesion and subsequent entrainment processes also have an important effect on the distribution of flow depth. In fact, in the case of low cohesive flows and thus entrainment processes dominated by ploughing, the maximum flow depth is located immediately at the avalanche front. In contrast, in the case of more cohesive flows, and therefore the dominance of abrasive entrainment processes, the maximum avalanche depth is located within the avalanche body.

The current literature suggests that three additional entrainment mechanisms may be at play in natural gravitational flows, in particular in snow avalanches: eruption, impact erosion, and secondary slab release (Gauer and Issler, 2004; Iverson et al., 2011; Köhler et al., 2018a; Sovilla et al., 2006). Although we believe that these mechanisms are very plausible in snow avalanches, our modelling approach does not yet include some key physical processes necessary for their modelling. In particular, our model does not include an interstitial fluid, which is the essential ingredient to be able to model eruption (Gauer and Issler, 2004; Iverson, 2012; Louge et al., 2011). In addition, we only model the dense part of the flow and therefore cannot reproduce entrainment processes such as impact erosion, which are known to be associated with the turbulent intermittent flow regime encountered in the suspended layers of powder snow avalanches (Köhler et al., 2018a; Sovilla et al., 2015). Finally, the release of secondary slabs along the path can also be a source of large localized entrainment rates. In the future, simulations of this mechanism could be achieved by discretizing the snowpack with layers of different cohesions and/or by simulating a weak snow layer (Bobillier et al., 2020). Note that here we do not distinguish between erosion and entrainment as is sometimes done, e.g. by (Li et al., 2022), because the entire depth of the bed is eventually mobilized within the flow at some point in our simulations. Thus, all the eroded particles are also entrained, which makes this distinction trivial.

4.3. Deposition

Our simulations show that the cohesive properties of snow also influence the deposition processes. Fig. 7 shows that the avalanche tail consists mostly of a mixture of particles from the initial released mass and the deeper layers within the bed, the latter being warmer and

therefore more cohesive snow (Steinkogler et al., 2015a; Steinkogler et al., 2015b). It is thus very probable that the material being deposited is characterized by high cohesion values. A sensitivity analysis performed on the $h_{\text{stop}}(\theta)$ curves in Fig. 9 shows an increase of the deposition height h_{stop} with increasing cohesion, suggesting that a cohesive material would enhance the detrainment at the avalanche tail. For example, for a slope angle of around 30° , the deposit thickness of cohesionless flows is around 0.4 m, while it is around 1.6 m for cohesive flows. However, this trend must be considered carefully in the specific case of snow avalanches. Indeed, the curves of $h_{\text{stop}}(\theta)$ are sensitive to the properties of the ground (e.g. friction and roughness), which in our case consists of the same particles as the flow, but may be totally different in reality, for example with the formation of a sliding surface at the bottom of the flow (Bartelt et al., 2012). The empirical expression for $h_{\text{stop}}(\theta)$ proposed by Pouliquen (1999) for dry granular flows seems to work as well with cohesive particles. The evolution of the fitting parameters θ_1 , θ_2 and L with regard to the bond strength seem relatively predictable, meaning that Eq. (4) could be expanded to include σ_{bond} . In this way, the deposition height could be anticipated, provided that we know the basal conditions of the flow.

5. Conclusion

Overall, the numerical experiments presented in this article demonstrate that the cohesion of the material greatly impacts the mass exchange between the flow and the erodible bed. Our simulations show that the ploughing mechanism dominates when bonds between particles are weak, while abrasion controls entrainment in the presence of strong bonds. We proposed a simple parameter allowing to differentiate between the two mechanisms and quantify the entrainment velocity as a function of cohesion. Mixing is also affected by cohesion, as the ploughing mechanism, typical of cohesionless flows, tends to maintain vertical bed structure within the flow, while abrasion promotes more mixing. At the tail of the flow, we evaluated the impact of cohesion on the deposition height, through the $h_{\text{stop}}(\theta)$ curves. We find that cohesion has a positive, non-linear, impact on h_{stop} . Because our simulations naturally mimic real mechanisms, escaping from forceful mathematical assumptions, we expect our findings to guide modellers of full-scale gravitational mass movements towards the development of a novel generation of physics-based entrainment models in practice-oriented depth-averaged approaches. The proposed model, although simplistic,

could be improved in the future to study additional avalanche processes. For instance, an extension to three dimensions would allow to study lateral effects, such as levee formation and fingering. In addition, the inclusion of an interstitial fluid (Li and Zhao, 2018) would provide a better understanding of the entrainment of water-saturated material (Iverson et al., 2011) or eruption mechanisms at the front of dry-snow avalanches.

Funding

CL and BS are funded by WSL's strategic initiative Climate Change Impacts on Alpine Mass Movements (CCAMM, ccamm.slf.ch) and the canton of Valais. JG is funded by the Swiss National Science Foundation (Eccellenza project: grant number PCEFP2_181227). The funders had no role in study design, data collection and analysis, decision to publish, or preparation of the manuscript.

Authors statement

We thank Dr. Dieter Issler for his very thorough review of our paper and his insightful comments.

CRediT authorship contribution statement

Camille Ligneau: Conceptualization, Data curation, Formal analysis, Investigation, Methodology, Software, Visualization, Writing – original draft, Writing – review & editing. **Betty Sovilla:** Conceptualization, Funding acquisition, Investigation, Methodology, Supervision, Writing – review & editing. **Johan Gaume:** Conceptualization, Formal analysis, Investigation, Methodology, Supervision, Writing – review & editing.

Declaration of Competing Interest

The authors declare that they have no known competing financial interests or personal relationships that could have appeared to influence the work reported in this paper.

Data availability

Data will be made available on request.

Appendix A. Bulk mechanical properties of the granular material

The parameters given in Table 2 define the cohesion between particles. However, the macroscopic mechanical properties of the bulk material still need to be characterized for a proper comparison with the properties of real snow. Therefore, we characterized the four types of snow scenarios using two numerical mechanical tests: a shear cell to get the failure envelope, and a planar Couette cell to investigate the rheology.

The shear cell test (Fig. A.1a) is similar to the one in Richefeu et al. (2006) used to investigate the shear strength properties of wet granular materials. The material is confined between a static container (in black), a mobile lid (in red) that can move horizontally, and a plate that pushes the material downwards (in green). A gradually increasing shear force T is applied on the mobile lid while a compressive force N is applied on the top plate. The resulting shear plane (dotted line) is then subjected to a normal stress $\sigma = N/S + \rho_b g H/2$ and a tangential stress $\tau = T/S$, where S is the horizontal cross-section of the container and H is the height of the sample. When τ reaches the material's shear strength τ_c , the stress drastically drops and the displacement of the mobile lid increases. For various N/S values in the range 0.5–10 kPa, we extract the values of τ_c and find the failure envelope $\tau_c = c + \sigma \tan \phi$ for each set of cohesion (Fig. A.2a).

The planar Couette cell (Fig. A.1b) is a common setup to investigate the $\mu(I)$ rheology of a granular material (da Cruz et al., 2005). Here, the material is confined between a static wall (in black) and a mobile wall (in red) allowed to move vertically and horizontally. Periodic boundary conditions are applied along the horizontal axis. Both walls are made of particles identical to the bulk particles. A confining pressure $\sigma = 10$ kPa and a horizontal velocity V_w are assigned to the moving wall, leading to the shearing of the material. The $\mu(I)$ rheology suggests, in this case, that the shear stress τ is proportional to the confining pressure σ as:

$$\tau = \mu_{\text{eff}}(I)\sigma \quad (\text{A.1})$$

where μ_{eff} is an effective bulk friction of the material, which depends on a dimensionless quantity, the so-called *inertial number* I , defined as:

$$I = \frac{\dot{\gamma} d_p}{\sqrt{\sigma/\rho_p}} \quad (\text{A.2})$$

with $\dot{\gamma} = V_w/L$ the mean shear rate. In the present work, we apply a constant pressure σ and vary the wall velocity V_w until a steady state is reached. The shear stress τ is then measured to obtain the effective friction μ_{eff} for a given I (Fig. A.2b).

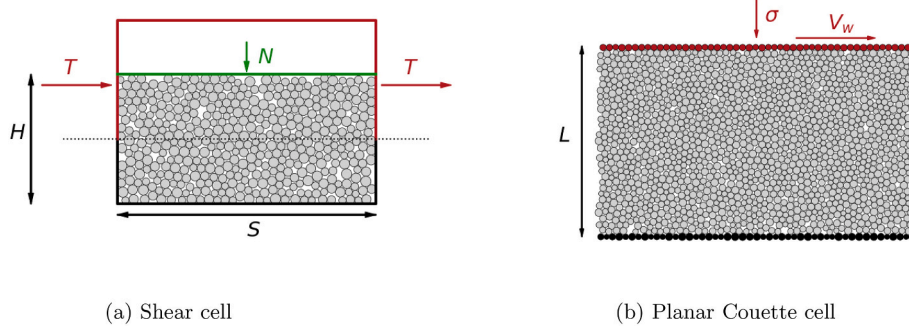


Fig. A.1. Setups of the mechanical tests: a shear cell (a) and a planar Couette cell (b).

The present paragraph presents a simple macroscopic characterisation of the simulated cohesive particles, for each of the four cases in Table 2. The failure envelope (Fig. A.2a) describes the maximum shear stress that the bulk material can sustain in a static state as a function of the normal stress. The shape of the failure envelope is almost linear, with an effective cohesion c for $\sigma = 0$ and an effective static friction $\tan\phi$. We observe that the *low adhesion–low strength* condition gives the weakest strength, with an effective cohesion of 500 Pa and an effective static friction angle of 28.6° . The strongest case is the *high adhesion–high strength*, with $c = 5$ kPa and $\phi = 48.4^\circ$. The two other situations seem to have a relatively similar failure envelope, considering the scattering of the data. They exhibit an effective cohesion of 3.5 kPa and 4.5 kPa, which is between the other two cases. However, their effective friction is similar to the one of the *low adhesion–low strength* case. Fig. A.2b displays the friction law $\mu(I)$, which characterises the effective friction μ_{eff} of the flowing material under shear. In general, we find that μ_{eff} is relatively stable for $I < 10^{-2}$ and increases with higher I values. The $\mu(I)$ curves for the two *low adhesion* cases are overlapping, considering the error bars. This makes sense as no bonds are supposed to be present between particles after a sufficiently long time of shearing, given that the low η_{agg} prevents new bonds from forming. The *high adhesion–low strength* case shows the same trend but has overall a greater effective friction. Finally, the *high adhesion–high strength* case exhibits an even higher effective friction, but seems to be less impacted by the increasing of I .

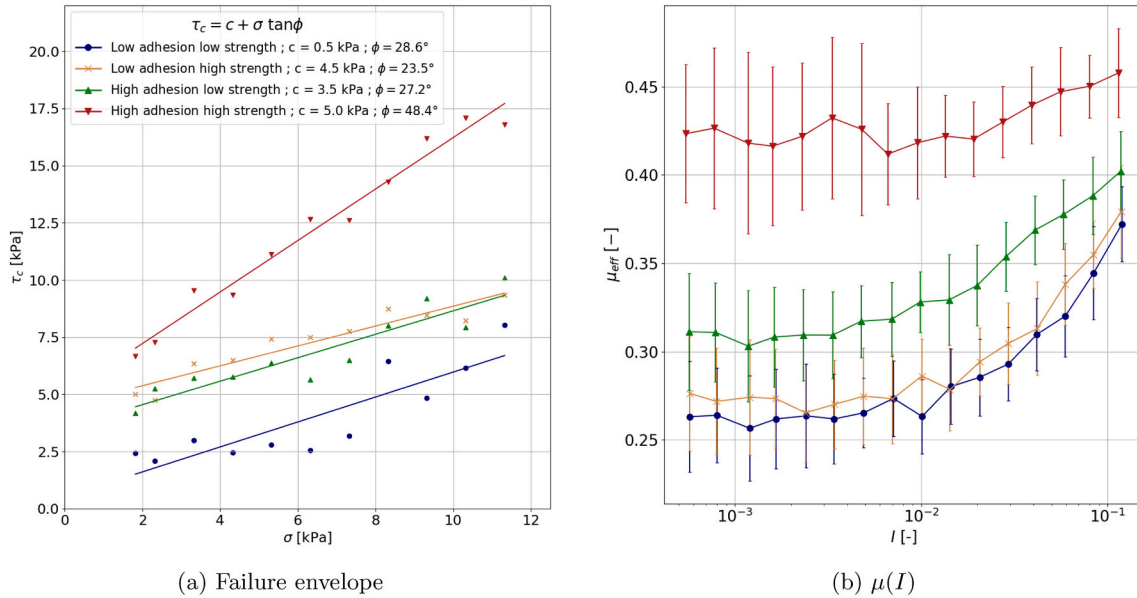


Fig. A.2. Mechanical tests. For the four cases of cohesion, the left panel shows the failure envelope and the right panel shows the friction law.

Appendix B. Computation of the granular temperature

For more details about the equations and notations provided below, the reader can refer to (Weinhart et al., 2013). The granular temperature T_g displayed in Fig. 8 is computed at a point \mathbf{r} and time t as:

$$T_g(\mathbf{r}, t) = \frac{\text{tr}(\boldsymbol{\sigma}_k(\mathbf{r}, t))}{2\rho(\mathbf{r}, t)} \quad (\text{B.1})$$

where ρ is the mass density field:

$$\rho(\mathbf{r}, t) = \sum_{\alpha=1}^N m_{\alpha} W(\mathbf{r} - \mathbf{r}_{\alpha}(t)) \quad (\text{B.2})$$

with m_{α} the mass of the particle α , N the total number of particles, \mathbf{r}_{α} the position of particle α and W the 2D Lucy function:

$$W(r < h) = \frac{5}{\pi h^2} \left[1 - 6 \frac{r^2}{h^2} + 8 \frac{r^3}{h^3} - 3 \frac{r^4}{h^4} \right] \quad W(r > h) = 0 \quad (\text{B.3})$$

with $h = 0.6d$.

The kinetic stress $\sigma_k(\mathbf{r}, t)$ is computed as:

$$\sigma_k(\mathbf{r}, t) = \sum_{\alpha=1}^N m_{\alpha} \mathbf{v}_{\alpha}' \mathbf{v}_{\alpha}' W(\mathbf{r} - \mathbf{r}_{\alpha}) \quad (\text{B.4})$$

with $\mathbf{v}_{\alpha}'(\mathbf{r}, t) = \mathbf{v}_{\alpha}(t) - \mathbf{V}(\mathbf{r}, t)$. The velocity field \mathbf{V} is calculated as follows:

$$\mathbf{V}(\mathbf{r}, t) = \frac{\mathbf{j}(\mathbf{r}, t)}{\rho(\mathbf{r}, t)} \quad (\text{B.5})$$

with the momentum density vector:

$$\mathbf{j}(\mathbf{r}, t) = \sum_{\alpha=1}^N m_{\alpha} \mathbf{v}_{\alpha} W(\mathbf{r} - \mathbf{r}_{\alpha}) \quad (\text{B.6})$$

References

- Bahaloo, H., Eidevåg, T., Gren, P., Casselgren, J., Forsberg, F., Abrahamsson, P., Sjö Dahl, M., 2022. Ice sintering: Dependence of sintering force on temperature, load, duration, and particle size. *J. Appl. Phys.* 131 (2), 025109. <https://doi.org/10.1063/5.0073824>.
- Barbolini, M., Biancardi, A., Cappabianca, F., Natale, L., Pagliardi, M., 2005. Laboratory study of erosion processes in snow avalanches. *Cold Reg. Sci. Technol.* 43 (1), 1–9. <https://doi.org/10.1016/j.coldregions.2005.01.007>.
- Bartelt, P., McDardell, B.W., 2009. Granulometric investigations of snow avalanches. *J. Glaciol.* 55 (193), 829–833. <https://doi.org/10.3189/002214309790152384>.
- Bartelt, P., Glover, J., Feistl, T., Bühler, Y., Buser, O., 2012. Formation of levees and enechelon shear planes during snow avalanche run-out. *J. Glaciol.* 58 (211), 980–992. <https://doi.org/10.3189/2012JoG11J011>.
- Bobillier, G., Bergfeld, B., Capelli, A., Dual, J., Gaume, J., Herwijnen, A.V., Schweizer, J., 2020. Micromechanical modeling of snow failure. *Cryosphere* 14 (1), 39–49. <https://doi.org/10.5194/tc-14-39-2020>.
- Bouchaud, J.-P., Cates, M.E., Prakash, J.R., Edwards, S.F., 1995. Hysteresis and metastability in a continuum sandpile model. *Phys. Rev. Lett.* 74 (11), 1982–1985. <https://doi.org/10.1103/PhysRevLett.74.1982>.
- Cicoira, A., Blatny, L., Li, X., Trottet, B., Gaume, J., 2022. Towards a predictive multi-phase model for alpine mass movements and process cascades. *Eng. Geol.* 310, 106866. <https://doi.org/10.1016/j.enggeo.2022.106866>.
- Cundall, P.A., Strack, O.D.L., 1979. A discrete numerical model for granular assemblies. *Géotechnique* 29 (1), 47–65. <https://doi.org/10.1680/geot.1979.29.1.47>.
- da Cruz, F., Emam, S., Prochnow, M., Roux, J.-N., Chevoir, F., 2005. Rheophysics of dense granular materials: Discrete simulation of plane shear flows. *Phys. Rev. E* 72 (2), 021309. <https://doi.org/10.1103/PhysRevE.72.021309>.
- Edwards, A.N., Viroulet, S., Johnson, C.G., Gray, J.M.N.T., 2021. Erosion-deposition dynamics and long distance propagation of granular avalanches. *J. Fluid Mech.* 915. <https://doi.org/10.1017/jfm.2021.34>.
- Eglit, M., Demidov, K., 2005. Mathematical modeling of snow entrainment in avalanche motion. *Cold Reg. Sci. Technol.* 43 (1–2), 10–23. <https://doi.org/10.1016/j.coldregions.2005.03.005>.
- Gauer, P., Issler, D., 2004. Possible erosion mechanisms in snow avalanches. *Ann. Glaciol.* 38, 384–392. <https://doi.org/10.3189/172756404781815068>.
- Gaume, J., Gast, T., Teran, J., van Herwijnen, A., Jiang, C., 2018. Dynamic anticrack propagation in snow. *Nat. Commun.* 9 (1), 3047. <https://doi.org/10.1038/s41467-018-05181-w>.
- Gaume, J., van Herwijnen, A., Gast, T., Teran, J., Jiang, C., 2019. Investigating the release and flow of snow avalanches at the slope-scale using a unified model based on the material point method. *Cold Reg. Sci. Technol.* 168, 102847. <https://doi.org/10.1016/j.coldregions.2019.102847>.
- GDR MiDi, 2004. On dense granular flows. *Eur. Phys. J. E* 14 (4), 341–365. <https://doi.org/10.1140/epje/i2003-10153-0>.
- Giacona, F., Eckert, N., Corona, C., Mainieri, R., Morin, S., Stoffel, M., Martin, B., Naaim, M., 2021. Upslope migration of snow avalanches in a warming climate. *Proc. Natl. Acad. Sci.* 118 (44). <https://doi.org/10.1073/pnas.2107306118>.
- Gray, J., Thornton, A., 2005. A theory for particle size segregation in shallow granular free-surface flows. *Proceed. Royal Soc. A* 461 (2057), 1447–1473. <https://doi.org/10.1098/rspa.2004.1420>.
- Grigorian, S., Eglit, M., Yakimov, Y., 1967. A new formulation and solution of the problem of the motion of a snow avalanche. *Trudy Vycokogornogo Geofizicheskogo Inst.* 12, 104–113.
- Grigorian, S.S., Ostroumov, A.V., 1977. *Matematicheskaya Model Sklonovih Processov Lavinnogo Tipa [The Mathematical Model for Slope Processes of Avalanche Type]*. Institute for Mechanics, Moscow State University, Moscow, Russia, Scientific Report, 1955.
- Issler, D., Pastor Pérez, M., 2011. Interplay of entrainment and rheology in snow avalanches: a numerical study. *Ann. Glaciol.* 52 (58), 143–147. <https://doi.org/10.3189/172756411797252031>.
- Issler, D., Gauer, P., Barbolini, M., Balean, R., 2000. Continuum models of particle entrainment and deposition in snow drift and avalanche dynamics. In: *Models of Continuum Mechanics in Analysis and Engineering. Proceedings of a conference held at the Technische Universität Darmstadt*, pp. 58–80. September. 30.
- Iverson, R.M., 2012. Elementary theory of bed-sediment entrainment by debris flows and avalanches. *J. Geophys. Res. Earth* 117 (F3). <https://doi.org/10.1029/2011JF002189>.
- Iverson, R.M., Reid, M.E., Logan, M., LaHusen, R.G., Godt, J.W., Griswold, J.P., 2011. Positive feedback and momentum growth during debris-flow entrainment of wet bed sediment. *Nat. Geosci.* 4 (2), 116–121. <https://doi.org/10.1038/ngeo1040>.
- Kadav, D., Herrmann, H.J., 2011. Density profiles of loose and collapsed cohesive granular structures generated by ballistic deposition. *Phys. Rev. E* 83 (3), 031301. <https://doi.org/10.1103/PhysRevE.83.031301>.
- Kang, C., Chan, D., 2018. Numerical simulation of 2D granular flow entrainment using DEM. *Granul. Matter* 20 (1), 13. <https://doi.org/10.1007/s10035-017-0782-x>.
- Köhler, A., McElwaine, J. N., & Sovilla, B. (2018a). GEODAR data and the flow regimes of snow avalanches. *J. Geophys. Res. Earth*, 123 (6), 1272–1294. <https://doi.org/10.1002/2017JF004375>.
- Köhler, A., Fischer, J.-T., Scandroglio, R., Bavay, M., McElwaine, J., Sovilla, B., 2018b. Cold-to- warm flow regime transition in snow avalanches. *Cryosphere* 12 (12), 3759–3774. <https://doi.org/10.5194/tc-12-3759-2018>.
- Kyburz, M.L., 2021. *Pressure on obstacles induced by granular snow avalanches* [Doctoral dissertation, EPFL]. In: Prof. Jean-François Molinari (président) ; Prof. Christophe Ancey, Dr Betty Sovilla (Directeurs); Prof. Mark Sawley, Prof. Nico Gray, Dr Thierry Faug (Rapporteurs).
- Kyburz, M.L., Sovilla, B., Gaume, J., Ancey, C., 2020. Decoupling the role of inertia, friction, and cohesion in dense granular avalanche pressure build-up on obstacles. *J. Geophys. Res. Earth* 125 (2). <https://doi.org/10.1029/2019JF005192>.
- Kyburz, M.L., Sovilla, B., Gaume, J., Ancey, C., 2022a. Physics-based estimates of drag coefficients for the impact pressure calculation of dense snow avalanches. *Eng. Struct.* 254, 113478. <https://doi.org/10.1016/j.engstruct.2021.113478>.
- Kyburz, M.L., Sovilla, B., Gaume, J., Ancey, C., 2022b. The concept of the mobilized domain: how it can explain and predict the forces exerted by a cohesive granular avalanche on an obstacle. *Granul. Matter* 24 (2), 45. <https://doi.org/10.1007/s10035-021-01196-1>.

- Li, W.C., Li, H.J., Dai, F.C., Lee, L.M., 2012. Discrete element modeling of a rainfall-induced flowslide. *Eng. Geol.* 149–150, 22–34. <https://doi.org/10.1016/j.enggeo.2012.08.006>.
- Li, X., Zhao, J., 2018. A unified CFD-DEM approach for modeling of debris flow impacts on flexible barriers. *Int. J. Numer. Anal. Methods Geomech.* 42 (14), 1643–1670. <https://doi.org/10.1002/nag.2806>.
- Li, X., Sovilla, B., Ligneau, C., Jiang, C., Gaume, J., 2022. Different erosion and entrainment mechanisms in snow avalanches. *Mech. Res. Commun.* 124, 103914. <https://doi.org/10.1016/j.mechrescom.2022.103914>.
- Ligneau, C., Sovilla, B., Gaume, J., 2022. Numerical investigation of the effect of cohesion and ground friction on snow avalanches flow regimes. *PLoS One* 17 (2), e0264033. <https://doi.org/10.1371/journal.pone.0264033>.
- Lo, C.-M., Lin, M.-L., Tang, C.-L., Hu, J.-C., 2011. A kinematic model of the Hsiaoalin landslide calibrated to the morphology of the landslide deposit. *Eng. Geol.* 123 (1), 22–39. <https://doi.org/10.1016/j.enggeo.2011.07.002>.
- Louge, M.Y., Carroll, C.S., Turnbull, B., 2011. Role of pore pressure gradients in sustaining frontal particle entrainment in eruption currents: the case of powder snow avalanches. *J. Geophys. Res. Earth* 116 (F4). <https://doi.org/10.1029/2011JF002065>.
- Mangeney, A., 2011. Landslide boost from entrainment. *Nat. Geosci.* 4 (2), 77–78. <https://doi.org/10.1038/ngeo1077>.
- Naaïm, M., Faug, T., Naaïm-Bouvet, F., 2003. Dry granular flow modelling including erosion and deposition. *Surv. Geophys.* 24 (5/6), 569–585. <https://doi.org/10.1023/B:GEOP.0000006083.47240.4c>.
- Naaïm, M., Eckert, N., Giraud, G., Faug, T., Chambon, G., Naaïm-Bouvet, F., Richard, D., 2016. Impact du réchauffement climatique sur l'activité avalancheuse et multiplication des avalanches humides dans les Alpes françaises. *La Houille Blanche* 6, 12–20. <https://doi.org/10.1051/lhb/2016055>.
- Obermayr, M., Vrettos, C., Eberhard, P., Däuwel, T., 2014. A discrete element model and its experimental validation for the prediction of draft forces in cohesive soil. *J. Terramech.* 53, 93–104. <https://doi.org/10.1016/j.jterra.2014.04.003>.
- Pielmeier, C., Techel, F., Marty, C., Stucki, T., 2013. Wet Snow Avalanche Activity in the Swiss Alps – Trend Analysis for Mid-Winter Season, p. 8.
- Potyondy, D.O., Cundall, P.A., 2004. A bonded-particle model for rock. *Int. J. Rock Mech. Min. Sci.* 41 (8), 1329–1364. <https://doi.org/10.1016/j.ijrmmms.2004.09.011>.
- Pouliquen, O., 1999. Scaling laws in granular flows down rough inclined planes. *Phys. Fluids* 11 (3), 542–548. <https://doi.org/10.1063/1.869928>.
- Richefeu, V., El Yousoufi, M.S., Radjai, F., 2006. Shear strength properties of wet granular materials. *Phys. Rev. E* 73 (5), 051304. <https://doi.org/10.1103/PhysRevE.73.051304>.
- Savage, S.B., Hutter, K., 1989. The motion of a finite mass of granular material down a rough incline. *J. Fluid Mech.* 199, 177–215. <https://doi.org/10.1017/S0022112089000340>.
- Sovilla, B., Burlando, P., Bartelt, P., 2006. Field experiments and numerical modeling of mass entrainment in snow avalanches. *J. Geophys. Res. Earth* 111 (F3). <https://doi.org/10.1029/2005JF000391>.
- Sovilla, B., McElwaine, J.N., Schaer, M., Vallet, J., 2010. Variation of deposition depth with slope angle in snow avalanches: Measurements from Vallée de la Sionne. *J. Geophys. Res. Earth* 115 (F2). <https://doi.org/10.1029/2009JF001390>.
- Sovilla, B., McElwaine, J.N., Louge, M.Y., 2015. The structure of powder snow avalanches. *C. R. Phys.* 16 (1), 97–104. <https://doi.org/10.1016/j.crhy.2014.11.005>.
- Steinkogler, W., Sovilla, B., Lehning, M., 2015a. Thermal energy in dry snow avalanches. *Cryosphere* 9 (5), 1819–1830. <https://doi.org/10.5194/tc-9-1819-2015>.
- Steinkogler, W., Gaume, J., Löwe, H., Sovilla, B., Lehning, M., 2015b. Granulation of snow: from tumbler experiments to discrete element simulations. *J. Geophys. Res. Earth* 120 (6), 1107–1126. <https://doi.org/10.1002/2014JF003294>.
- Takahashi, T., 2001. Mechanics and simulation of snow avalanches, pyroclastic flows and debris flows. In: *Particulate Gravity Currents*. John Wiley & Sons, Ltd, pp. 9–43. <https://doi.org/10.1002/9781444304275.ch2>.
- Thompson, N., Bennett, M.R., Petford, N., 2009. Analyses on granular mass movement mechanics and deformation with distinct element numerical modeling: Implications for large-scale rock and debris avalanches. *Acta Geotech.* 4 (4), 233–247. <https://doi.org/10.1007/s11440-009-0093-4>.
- Ucgul, M., Fielke, J.M., Saunders, C., 2014. Three-dimensional discrete element modelling of tillage: Determination of a suitable contact model and parameters for a cohesionless soil. *Biosyst. Eng.* 121, 105–117. <https://doi.org/10.1016/j.biosystemseng.2014.02.005>.
- Vicari, H., Tran, Q.A., Nordal, S., Thakur, V., 2022. MPM modelling of debris flow entrainment and interaction with an upstream flexible barrier. *Landslides* 19 (9), 2101–2115. <https://doi.org/10.1007/s10346-022-01886-8>.
- Viroulet, S., Edwards, A.N., Johnson, C.G., Kokelaar, B.P., Gray, J.M.N.T., 2019. Shedding dynamics and mass exchange by dry granular waves flowing over erodible beds. *Earth Planet. Sci. Lett.* 523, 115700. <https://doi.org/10.1016/j.epsl.2019.07.003>.
- Weinhart, T., Hartkamp, R., Thornton, A.R., Luding, S., 2013. Coarse-grained local and objective continuum description of three-dimensional granular flows down an inclined surface. *Phys. Fluids* 25 (7), 070605. <https://doi.org/10.1063/1.4812809>.